

Update of the Seismogenic Potential of the Upper Rhine Graben Southern Region

Sylvain Michel^{1,2}, Clara Duverger², Laurent Bollinger², Jorge Jara¹, Romain Jolivet^{1,3}

¹ Laboratoire de Géologie, Département de Géosciences, Ecole Normale Supérieure, PSL Université, CNRS UMR 8538, 24 Rue Lhomond, 75005, Paris, France.

² CEA, DAM, DIF, F-91297 Arpajon, France

³ Institut Universitaire de France, 1 rue Descartes, 75005, Paris

Correspondence to: Sylvain Michel (sylvain_michel@live.fr)

Abstract.

The Upper Rhine Graben (URG), located in France and Germany, is bordered by north-south trending faults, some of which are ~~them~~ considered active, posing a potential threat to ~~the~~ dense population and infrastructures ~~on from~~ the Alsace plain. The largest historical earthquake in the region ~~wais~~ the M6.5+/-0.5 Basel earthquake in 1356. Current seismicity ($M > 2.5$ since 1960) is mostly diffuse and located within the graben. We build upon previous seismic hazard studies of the URG by exploring uncertainties in greater detail ~~and~~, revisiting a number of assumptions. We first take into account the limited evidence of neotectonic activity, then explore tectonic scenarios that have not been taken into account previously, exploring uncertainties ~~for~~ M_{max} , its recurrence time, the b -value, and the moment released aseismically or through aftershocks. Uncertainties on faults' moment deficit rates, on the observed seismic events' magnitude-frequency distribution, and on the moment-area scaling law of earthquakes are also explored. Assuming a purely dip-slip / normal faulting mechanism associated to a simplified 3 main fault model, M_{max} maximum probability is estimated at M_w ~~6.105~~. Considering this scenario, there would be a 99% probability that M_{max} is ~~less than below 7.325~~. In contrast, ~~with~~ a strike slip assumption associated to a 4 main fault model, consistent with recent paleoseismological studies and the present-day stress field, M_{max} is estimated at M_w ~~6.8985~~. Based on this scenario, there would be a 99% probability that M_{max} is less than ~~7.655~~.

30 **1 INTRODUCTION**

31 The Upper Rhine Graben (URG), located in France and Germany, is bounded by north-south trending faults, some
32 of which are considered active, posing a potential threat to the dense population and the industrial and
33 communication infrastructures of the Alsace plain (Figure 1). The largest historical earthquake in the region ~~was~~
34 the 1356 Basel earthquake with a maximum intensity equal ~~to~~ or greater than IX (Mayer-Rosa and Cadiot, 1979;
35 Föh et al., 2009), an earthquake presently associated to a magnitude between $M_{6.5\pm 0.5}$ (Manchuel et al., 2017)
36 and $M_{6.9\pm 0.2}$ (Föh et al., 2009). Current seismicity ($M > 2.5$ since 1960) is mostly diffuse and located within the
37 graben (Dobre et al., 2022), hence the difficulty to attribute individual events to a given fault segment. The
38 bordering faults; themselves; are relatively quiet except for the south-eastern section of the graben, near Mulhouse-
39 Basel, where natural seismic sequences (ROULAND et al., 1983; Bonjer, 1997) and induced seismicity (Kraft and
40 Deichmann, 2014) ~~have~~ has been observed. Seismic activity actually varies along the URG with an increasing rate
41 of events towards the south (Barth et al., 2015). The relative rate between small and large events (b-value from the
42 Gutenberg-Richter law) ~~also~~ increases ~~also~~ towards the south indicating a surplus of small earthquakes or a deficit
43 of large events roughly south of Strasbourg (Barth et al., 2015). Focal mechanisms of earthquakes suggest that the
44 region ~~is subject to undergoes a~~ strike-slip regime with some normal component (Mazzotti et al., 2021),
45 consistent with the large wavelength strain inferred from geodetic data (Henrion et al., 2020). ~~Characterizing The~~
46 ~~characterization of~~ the slip rates of the graben's faults based on geodetic data remains challenging. Indeed regional
47 glacial isostatic adjustments, local subsidence and low tectonic strain rates result in a heterogeneous velocity field
48 with values below 0.2 mm/yr and often within measurement uncertainties (Fuhrmann et al., 2015; Henrion et al.,
49 2020).

50
51 ~~The seismic hazard of the URG has been evaluated by multiple studies at the national/European scale (Grünthal et~~
52 ~~al., 2018; Drouet et al., 2020; Danciu et al., 2021). Furthermore, the seismic hazard of the southern region of the~~
53 ~~URG in particular has recently been assessed by~~ ~~The seismic hazard of the URG southern region was recently~~
54 ~~assessed by~~ Chartier et al. (2017) ~~with a focus on the Fessenheim nuclear power plant with a particular focus on~~
55 ~~the nuclear plant of Fessenheim~~ (Figure 1). This study evaluates the seismic hazard ~~using~~ ~~with~~ a fault-based
56 approach, taking into account the network of potentially active ~~faults~~ ~~characterized~~ ~~characterized by~~ ~~fault of~~
57 Jomard et al. (2017). This fault-based work involves a moment budget approach, which ~~involves~~ ~~consists in~~
58 comparing the rate of moment release by seismicity and the rate of moment deficit (MDR) accumulating along

59 locked portions of faults between large earthquakes (i.e. the tectonic loading rate of each fault). Since the period
60 of seismological observation (a few centuries) is too short to be representative of the long-term behavior of
61 seismicity, Chartier et al. (2017) built instead a seismicity model assumed to be representative of the long-term
62 ~~M~~magnitude-~~F~~frequency ~~D~~distribution (MFD) of earthquakes, a method similarly used in
63 former studies (e.g. Molnar, 1979; Anderson and Luco, 1983; Avouac, 2015). Earthquakes below M_w ~~5~~5 are
64 disregarded (Bommer and Crowley, 2017; Chartier et al., 2017). Earthquakes between M_w ~~5~~5 and 6 are
65 assumed to follow the MFD of the catalog of earthquakes they consider. This catalog integrates several sources of
66 instrumental and historical earthquakes including sources from the *Laboratoire de Détection et de Géophysique*
67 of the *Commissariat à l'Énergie Atomique et aux énergies alternatives* (CEA-LDG; <http://www-dase.cea.fr/>) and
68 from the FPEC (French Parametric Earthquake Catalogue; Baumont and Scotti, 2011), the IRSN contribution to
69 SHEEC (SHARE European Earthquake Catalogue; Stucchi et al., 2013). ~~The~~ MFDs are estimated based on ~~within~~
70 a French seismotectonic zoning scheme defined by Baize et al. (2013). Earthquakes with magnitude above
71 M_w ~~6~~6 are assumed to occur on the fault planes (Jomard et al., 2017). Chartier et al. (2017) consider two types
72 of model: (1) Each fault ruptures only as its maximum magnitude event, which is controlled by the surface area of
73 the seismogenic fault segment (characteristic earthquake model); (2) Events follow the Gutenberg-Richter (GR)
74 law with a b-value equal to 1, and the maximum magnitude, M_{max} , is fixed as in the previous model. The
75 recurrence ~~time~~ of the M_w ~~>~~>6 events are then calibrated so that the rate of moment released by the
76 seismicity models matches the MDR estimated from neotectonic data (Chartier et al., 2017; Jomard et al., 2017).
77 The authors explore different fault geometries (e.g. dip and seismogenic depth) using a logic-tree methodology
78 and then proceed to the Probabilistic Seismic Hazard Assessment (PSHA) of the region, providing a map of the
79 probability of exceedance of Peak Ground Acceleration (PGA) within a time period.

80 ~~Within this framework, a~~ number of strong assumptions are ~~madetaken within this framework.taken~~. As
81 mentioned previously, a simplified fault network is used (Jomard et al., 2017), which constrains the seismogenic
82 area available for ruptures. Expert choices have also been made to distribute slip rates (i.e. loading rates) originally
83 attributed to faults that have been removed from the initial fault network (Nivière et al., 2008) on other fault
84 segments. On a number of faults, no estimates of neotectonic slip rate are available (e.g. West Rhenish Fault) and
85 the authors have chosen to apply slip rates equivalent to those from other nearby faults (0.01 to 0.05 mm/yr). The
86 neotectonic data are actually only along-dip slip rate estimates. No along-strike slip rates have yet been published
87 due to the lack of markers to quantify horizontal offsets along faults and ~~this such~~ component has thus been

Code de champ modifié

88 ~~ignored/neglected~~. In addition, Chartier et al. (2017) do not consider continuous probabilities as they apply a logic-
89 tree method. Chartier et al (2017) fix the b-value to 1, choose the seismogenic depth to be either 15 or 20 km and
90 do not take into account multi-segment ruptures ~~when to estimating~~ estimate a M_{max} for each fault segment.

91 In this study, we build upon Chartier et al. (2017) seismic hazard evaluation of the southern URG by exploring
92 uncertainties in greater detail, revisiting a number of assumptions. We ~~use/follow~~ the methodology from Rollins
93 and Avouac (2019) and Michel et al. (2021), which allows to evaluate the seismogenic potential of faults in a
94 probabilistic fashion and explore uncertainties ~~for/on~~ parameters such as the b-value or M_{max} . We use the fault
95 network and slip rates taken into account by Nivière et al. (2008), disregarding the Western Rhenish Fault for
96 which, ~~to our knowledge, no~~ slip rate ~~data information~~ is ~~un~~available. We assume faults can rupture
97 simultaneously (i.e. multi-segment rupture). In the following sections, we ~~start by first describing~~ describe the
98 concepts and methods we use to constrain the seismogenic potential of the URG, ~~and~~ then describe the data
99 available before discussing the robustness of our results.

100 2 METHOD

101 We ~~follow/use~~ the methodology from Michel et al. (2021) in order to estimate the seismogenic potential of the
102 upper Rhine Graben, including M_{max} and its recurrence time. As in Chartier et al. (2017), we produce seismicity
103 models representative of the long-term behavior of earthquakes. We assume that ~~the MFDs of~~ background
104 earthquakes ~~have a MFD that~~ follows a Gutenberg-Richter power law up to M_{max} . We define background
105 earthquakes as mainshocks, as opposed to their subsequent aftershocks. We assume that their timing of occurrence
106 is random, following a Poisson process. Each model is controlled by three parameters: (1) M_{max} , (2) the recurrence
107 time of events of a certain magnitude, τ_c , and (3) the b-value. We use two types of model, namely the tapered and
108 truncated models (Rollins and Avouac, 2019; Michel et al., 2021; [Figure S1](#)). The tapered model type assumes a
109 non-cumulative power-law MFD truncated at M_{max} , which ~~gives/give~~ rise to a tapered MFD in the cumulative
110 form (i.e. the traditional display when representing the Gutenberg-Richter law). The truncated model type assumes
111 instead a MFD with a distribution truncated at M_{max} in the cumulative form.

112 The seismicity models are then tested against three constraints: (1) the moment budget, as in Chartier et al. (2017),
113 which implies that moment released by slip on the fault should match the moment deficit accumulating between
114 earthquakes over a long period of time; (2) the moment-area scaling law, an empirical scaling law relating ~~for each~~
115 ~~earthquake the~~ rupture area to ~~the slip~~ ~~for each earthquake~~, and (3) the MFD of observed seismicity. ~~Each of these~~

116 ~~constraints are described in more detail in~~ the following sub-sections, ~~we describe in more detail each of those~~
117 ~~constraints.~~ The data and associated uncertainties used for the constraints are discussed in the following section
118 for (i.e. Section 3).

Mis en forme : Police : (Par défaut) Times New Roman, 10 pt, Anglais (États-Unis)

119 2.1 Moment budget

120 A moment budget consists in comparing the rate of moment released from slip events (seismic or aseismic),
121 \dot{m}_0^{Total} , with the moment deficit rate, \dot{m}_0^{def} , accumulating between slip events. The moment deficit rate is defined
122 by the equation $\dot{m}_0^{def} = \int \mu \dot{D}^{def} dA$, where μ is the shear modulus, A is the area that remains locked during the
123 interseismic period (i.e. the potential seismogenic zone), and \dot{D}^{def} is the rate at which slip deficit builds up. Since
124 ~~it is not yet possible in the URG to determine~~ the distribution of locked segments of faults and their associated
125 loading rates ~~cannot yet be determined for the URG~~ from geodetic measurements, A is assumed to be homogeneous
126 along-strike for each fault, while we consider possible the seismogenic width to change from one fault to another.
127 The rate at which slip deficit builds up, \dot{D}^{def} , is evaluated based on neotectonic information (see Section 3.1). The
128 total moment released, \dot{m}_0^{Total} is calculated based on the rate of moment release of the long-term seismicity model.
129 Since the long-term seismicity model only considers ~~only~~ mainshocks, we ~~included~~ include a fourth parameter,
130 α_s , that represents the proportion of moment released by background seismicity (Avouac, 2015), \dot{m}_0^{Bckgrd} , relative
131 to the total moment released (including aftershocks and aseismic afterslip). If $\dot{m}_0^{def} = \dot{m}_0^{Total} = \dot{m}_0^{Bckgrd} / \alpha_s$,
132 then the moment budget is said to be balanced.

133 The cumulative MFD ~~for~~ tapered and truncated seismicity models achieving a balanced ~~that balances the~~ moment
134 budget have an analytical form and are a function of M_{max} , b , \dot{m}_0^{def} and α_s (see Rollins and Avouac, 2019, and
135 references therein). We can therefore estimate the probability of a seismicity model balancing the moment budget,
136 P_{Budget} , by sampling the *a priori* distributions of those parameters.

138 2.2 Moment-area scaling law

139 According to global earthquake statistics, the moment released by an earthquake, m_0^{Seis} , is proportional to the area
140 of its rupture, A_{eq} , such ~~that as~~ that $m_0^{Seis} \propto A_{eq}^{3/2}$ (Wells and Coppersmith, 1994; Leonard, 2010; Stirling et al., 2013).
141 We use this scaling to evaluate whether a seismic event of a given magnitude has a rupture area that fits within the
142 seismogenic zone. By considering the spread ~~of~~ on the empirical distribution of magnitude vs. area, we assume

143 the probability distribution function of an event of magnitude M_w to be probable considering this scaling, $P_{scaling}$.
 144 We use here the self-consistent scaling law, and related uncertainties, as defined by Leonard (2010) in thes dip-
 145 slip equation (the strike-slip equation is in any case almost the same).

146 2.3 Earthquake catalog

147 We ~~finally~~ test whether the observed MFD from earthquake catalogs may be a sample of the distribution of the
 148 long-term seismicity models we are building. Effectively, we evaluate the likelihood of our observed MFD given
 149 the distribution of the models. Since we only consider ~~here only~~ mainshocks, ~~wewe~~. We define the likelihood of
 150 the observed seismicity catalog, P_{Cat} , as $P_{Cat} = \prod_i P_{poisson}^{M_i}$, where $P_{poisson}^{M_i}$ is the probability to observe $n_{obs}^{M_i}$
 151 events, within the magnitude bin M_i , occurring during the time period $t_{obs}^{M_i}$, assuming the long-term mean
 152 recurrence of events is $\tau_{model}^{M_i}$:

$$153 P_{poisson}^{M_i}(n_{obs}^{M_i}, t_{obs}^{M_i}, \tau_{model}^{M_i}) = \frac{(t_{obs}^{M_i}/\tau_{model}^{M_i})^{n_{obs}^{M_i}}}{(n_{obs}^{M_i})!} e^{-t_{obs}^{M_i}/\tau_{model}^{M_i}}.$$

154 Effectively, for a given seismicity model, we generate randomly 2500 declustered ~~earthquake catalogs of~~
 155 ~~earthquakes~~. We evaluate the likelihood of each catalog and define P_{Cat} as the average of these likelihood values.

156 Note that we follow the recommendation ~~by from~~ Felzer (2008) while exploring magnitude uncertainties and
 157 correct the magnitudes of for each event ~~their magnitude~~ by $\Delta M = (b^2 \sigma^2)/(2 \log_{10}(e))$, where b is the
 158 declustered catalog b -value, σ is the standard deviation ~~for of~~ the event's magnitude, and e is the exponential
 159 constant.

160 2.4 Seismicity model probability and marginal probabilities

161 Finally, the probability of a seismicity model is defined as $P_{SM} = P_{Budget} P_{Cat} P_{scaling}$ ~~$P_{parameters}$~~ which depends,
 162 among others, on M_{max} and b (Michel et al., 2021). The evaluation of the parameters to estimate P_{SM} are discussed
 163 in Section 3. Marginal probabilities such as $P_{M_{max}}$, the probability of M_{max} , and P_b , the probability of the b -value
 164 probability, can be estimated based on P_{SM} . We also define $P(\tau_{max} | M_{max})$ as the probability of the rate of M_{max} ,
 165 and $P(\tau | M_w)$ as the probability of the rate of events with magnitude M_w , which accounts for all earthquakes from
 166 all of the models (i.e. not only M_{max}). Probabilities needed for estimating seismic hazard (e.g. PSHA) such as the
 167 probability to have an event above magnitude M_w for a time period T , $P(M > M_w | T)$, can likewise be evaluated.

Mis en forme : Police :Anglais (Royaume-Uni)

168 **3 DATA AND ASSOCIATED UNCERTAINTIES**

169 We present in this section the data and their associated uncertainties used to evaluate each constraint.

170 **3.1 Neotectonic data, seismogenic along-dip width and moment deficit rate**

171 ~~In order to~~ evaluate the MDR for the moment budget constraint (Section 2.1), we must infer estimates of loading
172 rate (i.e. \dot{D}^{def}) for each fault taken into account. The slip rate on each fault is taken from Nivière et al. (2008) for
173 the Rhine River, Black Forest, Weinstetten and Lehen-Schonberg faults (the Landeck or West Renish faults are
174 not considered). Their slip rates rely on estimates of the cumulative vertical displacement of the faults based on
175 Pliocene-Quaternary sediments thickness variations measured from 451 boreholes, assuming that the
176 accommodation space opened by tectonic motion is completely balanced (or over-balanced) by sedimentation.
177 However, potential erosional periods due to the piracy of the Rhine River might bias the measurements, thus the
178 values are to be interpreted as maximum displacement estimates. ~~From the age of the sediments,~~ Nivière et al.
179 (2008) ~~inferred/infer~~ vertical slip rates of 0.07 and 0.17 mm/yr ~~from the age of the sediments~~ for the Rhine River
180 and Weinstetten faults, respectively. The Lehen-Schonberg fault slip ~~rate reaches is given~~ between 0.04 and
181 0.1 mm/yr. While borehole observations do not allow to conclude on the Pliocene-Quaternary slip rate of the Black
182 Forest fault, this structure is suggested to be inactive during this time period, and that the deformation is now
183 accommodated by the other ~~aforementioned~~ faults ~~aforementioned~~ (Nivière et al., 2008). Note that ~~these~~ these are
184 vertical slip rate estimates and ~~that~~ the along-strike component is for the moment neglected. For the moment rate
185 calculation, we project vertical slip rates on the along-dip direction considering the dip angles of each fault.

186 The seismogenic down-dip extent of a fault depends on the temperature gradient (e.g. Oleskevich et al., 1999),
187 among other parameters. Indeed, between the isotherms 350°C and 450°C, quartzo-feldspathic rocks undergo a
188 transition in frictional properties (Blanpied et al., 1995) from a rate-weakening (<350°C), potentially seismogenic
189 behavior to a rate-strengthening (>450°C), stable sliding behavior (Dieterich, 1979; Ruina, 1983). The geothermal
190 gradient below the URG is higher than ~~in~~ the surrounding regions due to its tectonic history (Freyermark et al.,
191 2017). Based on borehole temperature measurements from Guillou-Frottier et al. (2013), we estimate the envelopes
192 of the geothermal gradient in the southern URG (Figure S24), ~~assuming a linear temperature gradient with depth,~~
193 and show that the frictional property transition would occur between ~~depths of 6~~ (shallowest position of the 350°C
194 isotherm; Figure S2) and 18 km ~~depth~~ (deepest position of the 450°C isotherm; Figure S2). In this study, we define
195 the PDF of the seismogenic down-dip extent as a uniform distribution between 0 and 6 km depth associated ~~with~~
196 a linear taper down to 18 km. ~~The linearity of the taper implies that the position of the fault's transition to a fully~~

Mis en forme : Anglais (États-Unis)

Code de champ modifié

Mis en forme : Police : (Par défaut) Times New Roman, 10 pt, Anglais (États-Unis)

197 ~~rate-strengthening behavior (>350-450°C) has a uniform probability to fall between 6 km (shallowest position of~~
198 ~~the 350°C isotherm according to Figure S2) and 18 km depth (deepest position of the 450°C isotherm; Figure S2).~~

Mis en forme : Anglais (États-Unis)

199 ~~The linearity of the taper within the transition zone is not physics-driven and has been chosen arbitrarily.~~

200 Additionally, the southern part of the URG is the ~~site location~~ of a potash-salt evaporitic basin (Lutz and Cleintuar,
201 1999; Hinsken et al., 2007; Freymark et al., 2017), which reaches a maximum depth of ~2 km. Such
202 ~~formations~~formation may not accumulate any moment deficit as the yield stress of evaporites is very low (Carter
203 and Hansen, 1983). We assume each fault is potentially impacted by this formation, hence modulating the
204 seismogenic thickness and in turn the seismogenic area available for a rupture. The resulting PDF ~~for~~ the
205 seismogenic thickness is the convolution of the PDF of the down-dip extent of the seismogenic zone with the PDF
206 of the evaporitic basin thickness, ~~giving~~ a uniform distribution between 0 and 2 km. ~~Combining The combination~~
207 ~~of~~ both temperature and salt basin assumptions leads to a PDF of the along-dip seismogenic width, which is
208 uniform down to ~5 km and decreases linearly until ~17 km (Figures S32 to S65).

209 The moment deficit is then the product ~~of between~~ the length of each fault, their seismogenic width, the neo-
210 tectonic long-term slip rate, and the shear modulus that we fix to 30 GPa (same as in Chartier et al., 2017). Each
211 fault is assumed to have its own seismogenic width. The moment deficit rate of each fault is shown in Figure 1.
212 The PDFs ~~for~~ each of the fault's constitutive parameters are shown in Figure S32 to S65. ~~By c~~Considering the
213 range of the fault's geometrical parameters, which considers also the Black Forest Fault even though it is assumed
214 to be non-active, we obtain the moment-area constraint shown in Figure 2. ~~Events up to~~ $M_w 6.5$; ~~events are~~
215 equiprobable while those above $M_w 7.7$ are extremely improbable.

216 3.2 Instrumental and historical seismicity catalogs

217 ~~To constrain the MFD of the long-term seismicity models with an observational seismicity catalog, as described~~
218 ~~in Section 2.3, we need to evaluate from the observational catalog the number of events per magnitude bin $n_{obs}^{M_i}$~~
219 ~~over a period of time $t_{obs}^{M_i}$ (Section 2.3).~~ We use the earthquake catalog from Drouet et al. (2020) ~~to constrain the~~
220 ~~MFD of the long-term seismicity models (Section 2.3).~~ This catalog was built from multiple former catalogs. It
221 relies mostly on the FCAT-17 catalog (Manchuel et al., 2018), which is itself a combination of the instrumental
222 catalog SiHex (Sismicité de l'HEXagone; Cara et al., 2015) for the 1965-2009 period, and an historical catalog
223 based on the macroseismic database of SISFRANCE (BRGM, IRSN, EDF), intensity prediction equations from
224 Baumont et al. (2018) and the macroseismic moment magnitude determination from Traversa et al. (2018) for the

Mis en forme : Police :(Par défaut) Times New Roman, 10 pt, Couleur de police : Automatique, Anglais (États-Unis)

225 463-1965 period. Events ~~located more than beyond~~ 20 km ~~from of~~ the French border, not provided by the FCAT-
226 17, are based on the SHEEC catalog (Stucchi et al., 2013; Woessner et al., 2015). Finally, events ~~between from~~
227 2010 ~~and to~~ 2016 come from the CEA-LDG bulletins (<https://www-dase.cea.fr>). All events ~~magnitudes~~ ~~magnitude~~
228 are given in M_w and uncertainties are provided. Anthropogenic events are expected to be already removed from the
229 catalog (Cara et al., 2015; Manchuel et al., 2018).

230 We select events within the coordinates $[6^\circ, 8.5^\circ]$ ~~in~~ longitude and $[47^\circ, 49.5^\circ]$ latitude, *i.e.* a broad region covering
231 the whole URG, and divide the catalog ~~into in~~ two time periods, an instrumental ~~period~~ and an historical one taking
232 events from 1980 onwards and 1850 onwards, respectively. We decluster both catalogs to compare them ~~with to~~
233 the long-term seismicity models (Section 2.3). Declustering is based on the methodology of Marsan et al. (2017),
234 which evaluates the probability that an earthquake is a mainshock. Declustering is applied based on a completeness
235 magnitude, M_c , of 2.2 and 3.2 for the instrumental and historical catalogs, respectively (Text S1; Figures S76 and
236 S87). From the resulting catalogs, we keep events from 1994 onwards and 1860 onwards for the instrumental and
237 historical ~~catalogs~~ ~~catalog~~, respectively (Figures S76 and S87), in order to avoid border effects from declustering.
238 For the instrumental catalog, 1994 is also the date from which ~~the~~ seismicity rate appears relatively constant
239 (Figure S76). We then select events in the region of interest (*i.e.* the southern part of the URG), taking into account
240 only earthquakes located within a 10 km buffer around the faults considered, including the Black Forest fault
241 (Figure 3). Note that since no events ~~are considered~~ below M_c ~~are considered~~, there is a lack of events which falls
242 in the magnitude bins directly above M_c while exploring magnitude uncertainties. Thus, when applying the
243 earthquake catalog constraint (Section 2.3), we take events with $M_w \geq 2.875$ and $M_w \geq 4.325$ for the
244 instrumental and historical catalogs, respectively (Felzer, 2008) (Figure 3).

245 3.3 ~~Seismicity model~~ Constitutive parameters of the seismicity models

246 As mentioned in Section 2.1, the cumulative MFD ~~for of~~ tapered and truncated seismicity models balancing the
247 moment budget can be defined as a function of M_{max} , b , m_0^{def} and α_s . We explore ~~these~~ ~~these~~ parameters ~~using~~
248 ~~through~~ a grid search with M_{max} and b sampled uniformly over $M_{max} \in \mathcal{U}(4.5, 9.9)$ and $b \in \mathcal{U}(0.1, 1.45)$,
249 respectively. Based on global statistics of the post-seismic response following earthquakes (Alwahedi and
250 Hawthorne, 2019; Churchill et al., 2022), we assume ~~that~~ the PDF of α_s is a Gaussian distribution with
251 $\mathcal{N}(0.9, 0.25)$ ~~(90% 0.9, 25% 0.25)~~ (Figure S98). Finally, the PDF of the MDR ~~for of~~ each fault is assumed ~~to be~~
252 ~~uniform~~ ~~uniform~~ between 0 and the estimate based on the maximum slip rate from Nivière et al. (2008) (Section
253 3.1). We thus include scenarios for which almost no moment deficit accumulates on the fault (*i.e.* the fault slips

Code de champ modifié

254 aseismically or ~~accumulates~~ ~~accommodates~~ ~~accommodates~~ no strain over long periods of time). This ~~assumption~~
255 ~~hypothesis~~ contrasts with the choice ~~made by~~ ~~from~~ Chartier et al. (2017) who assume ~~that~~ each fault is fully locked
256 over a seismogenic width terminating at either 15 or 20 km. Doing so, we explore a broad range of possible models.

Mis en forme : Police :Anglais (États-Unis)

Mis en forme : Police :Anglais (États-Unis)

Mis en forme : Police :Anglais (États-Unis)

257 4 RESULTS

258 The combination of constraints (Section 2) leads to the results shown in Figure 4. For the truncated model, the
259 marginal probability of P_{SM} in the M_{max} and τ_{max} ~~space~~ is represented by the gray shaded distribution in Figure
260 4 (not shown for the tapered model since the models taper at M_{max}). The marginal probability of M_{max} for the
261 tapered model (in green) peaks at 6.105, while the one for the truncated model (in blue) is bi-modal with peaks at
262 5.452 and 5.875. For the truncated model (not the tapered model for the same reason as previously indicated), the
263 marginal probability $P(\tau_{max} | M_{max} = 5.875)$ (solid blue line in the y-axis) peaks at ~1000 yrs. Taking
264 $M_{max} = 6.556$ or ~~76.957.0~~, a number close to the estimated magnitude of the 1356 Basel earthquake, the marginal
265 probability would instead peak at ~16,000 and ~80,000 yrs, respectively.

266 The marginal probabilities $P(\tau | M_w = 6.105)$ and $P(\tau | M_w = 5.875)$ for the tapered and truncated models
267 (green and blue dotted lines on the y-axis, respectively), which take all events ~~from~~ of the seismicity models into
268 account (not only M_{max}), have instead peaks at ~16,000 yrs and ~10,000 yrs, respectively. The marginal
269 probability P_b peaks at ~0.85 and 0.9 for the tapered and truncated models, respectively.

270 The effect with and without the moment-area scaling law is shown in Figure 5. Adding the scaling law constraint
271 does not change the mode of $P_{M_{max}}$ but completely rejects scenarios with $M_{max} > 7.8$.

272 Finally, the probabilities $P(M > M_w | T)$ for $T = 100$ and 10,000 yrs are also shown in Figure 5. As an example,
273 the probability of occurrence for an event above $M_w 6.5$ (similar to the 1356 Basel earthquake) for an observational
274 period of 100 yrs is ~0.1% for both the tapered and truncated models. For an event above $M_w 6.0$ and for the same
275 period, ~~this probability is~~ ~~it is~~ instead ~1% for both models (see zoom in Figure 5.c).

276 ~~The correlations between M_{max} , the moment deficit rate, the b -value, and α_s , for both the tapered and truncated~~
277 ~~models but without the scaling law constraint, are shown in Figures S10 and S11. For both models, probable M_{max}~~
278 ~~increases with increasing b -value (Figure S10.a and S11.a), highlighting a strong interdependency between the~~
279 ~~two both parameters. Raising the moment deficit rate will control the minimum- probable M_{max} probable (Figures~~
280 ~~S10.b and S11.b) but will also tend to exclude reject scenarios with a high b -value (> 1.25 ; Figures S10.f and S11.f).~~

Mis en forme : Non Surlignage

Mis en forme : Non Surlignage

Mis en forme : Non Surlignage

Mis en forme : Non Surlignage

Mis en forme : Police :Non Surlignage

Mis en forme : Police :Non Surlignage

Mis en forme : Non Surlignage

281 While other trends are expected between the parameters are expected, they seem less visible, likely due to the
282 uncertainties of the parameters explored.

Mis en forme : Police :Non Surlignage

Mis en forme : Police :Non Surlignage

Mis en forme : Police :

283 The results if we combine the PDFs from the tapered and truncated models using a mixture distribution are shown
284 in Figure S12. $P_{M_{max}}$ has a main peak at 5.9 and a smaller peak at 5.2, which originates from the truncated model.
285 $P(\tau | M_w = 5.9)$ peaks instead at ~13 000 yrs.

Mis en forme : Police :Non Surlignage

Mis en forme : Police :

Mis en forme : Police :

Mis en forme : Police :

Mis en forme : Police :

Mis en forme : Police :

Mis en forme : Police :

Mis en forme : Police :

286 5 DISCUSSION

287 5.1 Sensibility to earthquake catalog declustering

288 The catalog declustering (i.e. removal of aftershocks) may have a significant impact on the results (Section 2.3),
289 influencing the shape of the observed MFD of earthquakes. We use in this study, we applied the methodology of
290 from Marsan et al. (2017), which is based on the ETAS framework and intrinsically assumes that background
291 events have a Poisson behavior. Other declustering methodologies are available and we test here the one from
292 Zaliapin and Ben-Zion (2013) based on the nearest-neighbor distances of events in the space-time-energy domain.
293 The results from this methodology produce background seismicity catalogs with more events than the one from
294 Marsan et al. (2017) (Text S2 and Figures S9-S13 to S14), but infers larger b-values when combining the
295 instrumental catalog with the historical one (as inferred by Figure 6.b). The analysis of the seismicogenic
296 potential of the URG using Zaliapin and Ben-Zion (2013) methodology results with $P_{M_{max}}$ peaking at $M_{6.325}$ for
297 the tapered model, and is still being bi-modal for the truncated model, with peaks at $M_{5.15-2}$ and $M_{5.85-9}$ (Figure
298 6). Unlike with Marsan et al. (2017), the second peak at lower magnitude for the truncated model is more probable
299 than the first one at larger magnitude. The most probable M_{max} for both models are thus slightly higher shifted to
300 lower magnitudes than the values ones estimated using Marsan et al. (2017) methodology, but the width of the
301 PDFs appears unchanged seem to have remained to within one first order of magnitude first order the same. The
302 resulting marginal probabilities $P(\tau | M_w = 5.6-15.9)$ and $P(\tau | M_w = 5.885)$ for the tapered and truncated
303 models have both peaks at ~825,000 yrs and ~12,500 yrs, respectively.

304 5.2 Source of seismicity

305 We initially selected earthquakes within a 10 km buffer zone around the faults to as it reflects the strain-spatial
306 strain pattern of a vertical fault blocked down to a depth of 10 km depth. Nevertheless, the locking depth could
307 potentially be deeper, down to ~18 km as suggested in Section 3.1. In this respect, regard, we We thus also provide

308 ~~the results if events are selected~~~~ingselecting events~~ within 20 km ~~of from~~ the faults (Figures ~~S12-S16~~ and ~~S13-S17~~).
309 Under these conditions, ~~the~~ seismicity rates of the observational earthquake catalogs are higher and ~~thus~~ constrain
310 the long-term seismicity models to cases that produce higher moment release rate. $P_{M_{max}}$ ~~thus~~ favours ~~thus~~ events
311 ~~with a of~~ lower magnitude than the one using events within 10 km (Figure 5; Section 4). The tapered model peaks
312 at M_w 5.985, instead of 6.105, while the truncated model ~~has two peaks~~ ~~twice~~ at M_w 5.215 and 5.8, ~~in a~~ ~~75~~, very
313 similar ~~manner~~ to the reference scenario in Section 4, except that the peak at M_w 5.215 is now the most probable.

314 However, current seismicity in the URG is seemingly diffuse and it is difficult to associate it with a fault in
315 particular (Dobre et al., 2022). On the other hand, geodetic data are not yet able to resolve any tectonic
316 deformation and thus to evaluate the loading rate of faults (Henrion et al., 2020). Even though the Drouet et al.
317 (2020) catalog, based on FCAT-17 catalog, is supposedly devoid of anthropic seismicity (Cara et al., 2015;
318 Manchuel et al., 2018), one can then ask whether the current seismicity is totally representative of the undergoing
319 long-term tectonic processes or presently modulated by surface loads such as the post-glacial rebound (e.g. Craig
320 et al., 2016), aquifer loads, erosion or incision (e.g. Bettinelli et al., 2008; Steer et al., 2014; Craig et al., 2017). If
321 so, the ~~assumption hypothesis stating~~ that the main driver of seismicity is tectonic loading breaks down and our
322 method ~~used to assess for assessing~~ seismic hazard must be completed by physics-based constraints of such
323 transient stress release (Calais et al., 2016). Distinguishing seismic sources triggered by tectonic loading from
324 other driven forces is an extremely difficult task. The earthquake catalog contribution (Section 2.3) might then not
325 be appropriate.

326 Additionally, the ~~magnitudes~~~~magnitude~~ of historical events from the FCAT-17 catalog (before the 1960s), and
327 thus the ~~ones~~~~one~~ from Drouet et al. (2020), seem to be overestimated (or ~~instead~~ the instrumental events have
328 underestimated magnitudes even though it seems less probable) and a bias of the MFD is thus expected (Beauval
329 and Bard, 2022; Dobre et al., 2022). For the URG case, 3 bins out of 7 of the observed MFD are estimated from
330 the instrumental period. The ~~bins~~~~ones~~ estimated from the historical period have thus slightly more weight in the
331 catalog constraint (Section 2.3).

332 We test an alternative constraint inferring that the possible magnitude and frequency of M_{max} must be consistent
333 with the observed largest event over the observation period (~146 yrs), meaning that it has to be larger than or
334 equal to the known largest event while the return period of the largest event cannot be significantly ~~shorter~~ ~~smaller~~
335 than the observation period (Approach 2 from Michel et al., 2018). This constraint is equivalent to
336 ~~considering~~~~consider~~ that there is no earthquakes ~~with a of~~ magnitude ~~greater than~~ ~~over~~ the largest event seen in

Code de champ modifié

Mis en forme : Néerlandais (Pays-Bas)

Mis en forme : Néerlandais (Pays-Bas)

the observation period ~~occurred~~ occurring during the time period ~~covered by~~ of the observed catalog. Theoretically, this constraint imposes a lower bound on M_{max} and its recurrence time. The results ~~obtained~~ using this constraint together with the moment budget and scaling law ones are shown in Figure 7. Since M_{max} frequency ~~differs for~~ is different between the tapered and truncated models, the new constraint imposes different lower bounds ~~for~~ on the two models. ~~The~~ truncated model ~~rejects~~ rejecting more strongly scenarios with M_{max} below ~~M_w 5.5 more strongly~~ M_w 5.5. P_b is not constrained by the observed seismicity catalog but higher values of the b -value seem slightly more probable (inset ~~in~~ Figure 7). The marginal probabilities $P(\tau | M_w = 5.985)$ and $P(\tau | M_w = 6.325)$ for the tapered and truncated models have peaks at ~12,500 yrs and ~63,000 yrs, respectively.

5.3 Strike slip component

In this study, as well as in Chartier et al. (2017), we assume solely along-dip displacement since it is the only published neo-tectonic information available. Nevertheless, recent paleo-seismological data ~~on~~ the Black Forest fault ~~near Karlsruhe (north of our study area)~~ suggest ~~2-5.9~~ m of cumulative strike-slip, in contrast to ~~10.3-0.6~~ 1.2 m of cumulative vertical slip, ~~over~~ in for an event that occurred after the last glacial maximum (~15,000 yrs in the last 5.9 ~~kayrs~~ kyr) (Pena-Castellnou et al., 2023). ~~Those~~ There are also evidence of other events with left-lateral slip, associated with vertical 0.5 m displacement ~~those~~ displacements seem to be associated with at least three paleo-earthquakes. ~~This~~ It suggests ~~earthquake~~. It suggest (1) that the Black Forest fault has been active during the Quaternary period and that (2) strike-slip might be predominant. The ratio between strike- and dip-slip from the Black Forest event would be then ~~equal to 4~~ between 3.3 and 6.64.8. We thus test a scenario where the Black Forest fault is associated with a maximum vertical slip deficit rate of 0.18 mm/yr, as proposed by Jomard et al. (2017), and where we multiply the maximum slip deficit rate of all ~~faults~~ considered ~~faults~~ by ~~46.64.8~~ (the largest strike-over dip slip ratio suggested). The results and the revised MDR ~~for~~ of each fault are shown in Figures 8 and S184. $P_{M_{max}}$ peaks at ~~M_w 6.46.85-8~~ and ~~M_w 6.46.65-6~~ for the tapered and truncated models, respectively. They are associated with the marginal probabilities $P(\tau | M_w = 6.885)$ and $P(\tau | M_w = 6.665)$ that both peak at ~16,000 yrs for the tapered and truncated models, ~~respectively~~. Note that ~~Pena-Castellnou et al. (2023)~~ suggest that earthquakes of potentially M_w 6.5 occurred north of our study area using Wells and Coppersmith (1994) equation between moment magnitude and average slip/maximum slip, the 2 m amount of strike slip estimated by ~~(Pena-Castellnou et al., (2023))~~ Castellnou et al. (2022) would suggest a ~~~ M_w 7.3/7.0~~. P_b peaks at 0.65 and 0.7

365 for both the tapered and truncated models, ~~respectively~~, thus at lower values than taking into account the vertical-
366 slip component alone.

367 The previous scenario tested (Figure 8) takes two more faults (i.e. Weinstetten and Lehen-Schonberg faults) into
368 account than in Chartier et al. (2017), as ~~these~~ these two faults are not present within the BDFFA (the French
369 database of potentially active faults; Jomard et al., 2017). The results obtained by selecting faults as defined by
370 ~~following~~ Chartier et al. (2017) ~~fault selection~~ and applying the strike slip assumption are provided in Figure S195.
371 $P_{M_{max}}$ peaks at ~~M_w 6.46-7.5-7~~ and ~~M_w 6.46-5.5-6~~ for the tapered and truncated models, respectively, very similar
372 to the scenario taking all four faults, as the moment deficit rate is dominated by the Rhine River and Black Forest
373 faults. Note that the marginal probabilities $P(\tau | M_w)$ and $P(\tau_{max} | M_{max})$ seem to get more noisy, likely due to
374 the shape of the MDR PDF which skews heavily towards zero (black line in Figure S184.e).

375 5.4 Multi-segment rupture

376 In this study we assume that all faults can rupture simultaneously. Nevertheless, the Black Forest Fault is initially
377 taken as ~~in~~ ~~none~~ active, and the traces of the Weinstetten and Lehen-Schonberg faults are separated by at least
378 ~~a minimum of~~ 7.9 km. According to Wesnousky (2006), multi-segment ruptures are associated with low
379 probability when the inter segment distance exceeds 5 km. Consequently, the seismogenic potential scenario from
380 Section 4 would ~~then~~ be an overestimation. On the other hand, according to Castellnou et al., 2022, the Black
381 Forest Fault is in fact active and seismogenic, and could be assumed to rupture with other faults. Additional
382 structures might actually link all the faults together (e.g. Lutz and Cleintuar, 1999; Bertrand et al., 2006; Rotstein
383 and Schaming, 2011). In this case, the seismogenic potential scenario from Section 4 would be interpreted as an
384 underestimation.

385 Finally, we only consider the faults within a finite zone, which controls the total seismogenic area of the faults (i.e.
386 the moment-area scaling law effect), whereas the faults continue northwards and southwards to a lesser extent.
387 According to Weng and Yang (2017), the aspect ratio (width to length ratio of the rupture's ~~width over length~~)
388 of dip-slip events ~~barely almost doesn't reaches~~ reach beyond 8. Taking a seismogenic width of 18 km (our
389 maximum estimate), the maximum length of earthquakes would then be 144 km, while the full length of the URG
390 ~~faults considered~~ faults, including the Black Forest fault ~~included~~, is ~250 km (~160 km if the Black Forest fault
391 is not included). The rupture of all the faults would then be unlikely. On the other hand, strike-slip events do not
392 seem to be capped by any aspect ratio (Weng and Yang, 2017), so $M_w > 7.5$ events cannot ~~then~~ be excluded in this
393 context.

394 **6 CONCLUSION**

395 In this study, we investigate the seismogenic potential of the south-eastern URG, building upon the work by
396 ~~from~~ Chartier et al. (2017). Based on a complex fault network (Nivière et al., 2008), we evaluate scenarios that
397 have not been accounted for previously, exploring uncertainties on M_{max} , its recurrence time, the b -value, and
398 the moment released aseismically or through aftershocks (see Table 2 for a summary of the results considering
399 the different scenarios). Uncertainties ~~for~~ the MDR, the observed MFD, and ~~on~~ the moment-area scaling law
400 are also explored. Given the four faults considered, and the scenario in which the Black Forest fault is no longer
401 active but where the other faults can still rupture simultaneously, the M_{max} maximum probability is estimated at
402 M_w 6.95-1 and M_w 5.75-8 using the tapered or the truncated seismicity models, respectively. Nevertheless, $P_{M_{max}}$
403 for the truncated model has a second peak at M_w 5.15-2 and the recurrence time of events of such magnitude (not
404 only M_{max}), $P(\tau | M_w = 5.215) \sim 2,000$ yrs, is much shorter ~~lower~~ than the one estimated using the main peak,
405 $P(\tau | M_w = 5.875) \sim 10,000$ yrs. ~~Again~~ Still considering the scenario ~~excluding~~ ~~ignoring~~ the Black Forest fault,
406 there ~~is~~ would be a 99% probability that M_{max} is less than below 7.25-3 using either the tapered or truncated
407 ~~models~~ model. ~~In contrast,~~ In contrast, when strike-slip kinematics are considered as described in Section 5.3
408 and the Black Forest Fault is taken into account, there is a 99% probability that M_{max} is less than 7.6 and 7.5 for
409 the tapered and truncated models, respectively. This is our preferred scenario as it is based on recent findings for
410 strike-slip mechanisms, although the assumptions made in this analysis are debatable (i.e. strike-slip/dip-slip
411 ratio evaluated on a fault just north of our zone of study and applied to all faults; Section 5.3). It should be noted
412 that seismic hazard studies often place an upper bound on the values of M_{max} considered. In the case of the
413 URG, studies that use varying approaches to ours, have yielded values comparable to, or marginally lower than
414 the 99th percentile of $P_{M_{max}}$ of our strike-slip scenario (e.g. M7.4, M 7.1 and M7.5 for Grunthal et al., 2018,
415 Drouet et al., 2020, and Danciu et al., 2021, respectively), considering strike-slip as described in Section 5.3 and
416 taking the Black Forest Fault into account, there ~~is~~ would be a 99% probability that M_{max} is less than below 7.55
417 for both models. ~~scenario is based on~~ ~~mechanisms~~ ~~assumptions~~ ~~made~~

418 In any case, within this study, strong assumptions still had to be made that certainly ~~affected~~ ~~afect~~ the results. It
419 includes the methodology used to decluster the earthquake catalogs, ~~on~~ determining whether it is wise to compare
420 a comparison between the loading rate of each fault and with seismicity is wise, ~~on~~ opting to only considering only
421 the dip-slip component despite the fact that while strike-slip is highly probable, ~~on~~ covering the possibility of
422 multi-segment ruptures and even the choice of the faults to ~~be considered,~~ ~~consider~~. Further work, from paleo-

Mis en forme : Gauche, Espacement automatique entre les caractères asiatiques et latins, Espacement automatique entre les caractères asiatiques et les chiffres

Mis en forme : Anglais (États-Unis)

Mis en forme : Police :(Par défaut) Times New Roman, Anglais (États-Unis)

Mis en forme : Anglais (États-Unis)

Mis en forme : Anglais (États-Unis)

Mis en forme : Police :(Par défaut) Times New Roman, Anglais (États-Unis)

Mis en forme : Anglais (États-Unis)

Mis en forme : Police :(Par défaut) Times New Roman, Anglais (États-Unis)

Mis en forme : Anglais (États-Unis)

Mis en forme : Police :(Par défaut) Times New Roman, Anglais (États-Unis)

Mis en forme : Anglais (États-Unis)

Mis en forme : Police :(Par défaut) Times New Roman, Anglais (États-Unis)

Mis en forme : Anglais (États-Unis)

Mis en forme : Police :(Par défaut) Times New Roman, Anglais (États-Unis)

Mis en forme : Anglais (États-Unis)

Mis en forme : Police :(Par défaut) Times New Roman, Anglais (États-Unis)

Mis en forme : Anglais (États-Unis)

Mis en forme : Anglais (États-Unis)

423 seismology, seismic reflection, geodesy, or earthquake relocation is needed to ~~obtain extract~~ more information on
424 the structures tectonically involved and their associated loading ~~rates~~rate, and to better constrain the URG seismic
425 hazard. ~~Longer time series on all the fields mentioned above might also help in this matter.~~

426 **7 CODE AVAILABILITY**

427 **8 DATA AVAILABILITY**

428 **9 AUTHOR CONTRUBUTION**

429 **10 COMPETING STATEMENT**

430 The authors acknowledge there are no conflicts of interest recorded.

431 **11 ACKNOWLEDGEMENT**

432 This work received funding from the European Research Council (ERC) under the European Union 's Horizon
433 2020 research and innovation program (Geo-4D project, grant agreement 758210). RJ acknowledges funding
434 from the Institut Universitaire de France.

435

436

Mis en forme : Police :Times, 10 pt, Français (France)

Mis en forme : Espace Avant : Automatique, Après :
Automatique, Interligne : simple

12 REFERENCES

- 437
438 Alwahedi, M. A., and J. C. Hawthorne, 2019, Intermediate-Magnitude Postseismic Slip Follows Intermediate-
439 Magnitude (M 4 to 5) Earthquakes in California, *Geophys. Res. Lett.*, 46, no. 7, 3676–3687, doi:
440 10.1029/2018GL081001.
- 441 Anderson, J. G., and J. E. Luco, 1983, Consequences of slip rate constraints on earthquake occurrence relations,
442 *Bull. - Seismol. Soc. Am.*, 73, no. 2, 471–496, doi: <https://doi.org/10.1785/BSSA0730020471>.
- 443 Avouac, J.-P., 2015, From Geodetic Imaging of Seismic and Aseismic Fault Slip to Dynamic Modeling of the
444 Seismic Cycle, *Annu. Rev. Earth Planet. Sci.*, 43, doi: 10.1146/annurev-earth-060614-105302.
- 445 Baize, S., E. M. Cushing, F. Lemeille, and H. Jomard, 2013, Updated seismotectonic zoning scheme of
446 Metropolitan France, with reference to geologic and seismotectonic data, *Bull. la Société Géologique Fr.*,
447 184, no. 3, 225–259, doi: 10.2113/gssgfbull.184.3.225.
- 448 Barth, A., J. R. R. Ritter, and F. Wenzel, 2015, Spatial variations of earthquake occurrence and coseismic
449 deformation in the Upper Rhine Graben, Central Europe, *Tectonophysics*, 651–652, 172–185, doi:
450 10.1016/j.tecto.2015.04.004.
- 451 Baumont, D., K. Manchuel, P. Traversa, C. Durouchoux, E. Nayman, and G. Ameri, 2018, Intensity predictive
452 attenuation models calibrated in Mw for metropolitan France, *Bull. Earthq. Eng.*, 16, no. 6, 2285–2310,
453 doi: 10.1007/s10518-018-0344-6.
- 454 Beauval, C., and P. Bard, 2022, History of probabilistic seismic hazard assessment studies and seismic zonation
455 in mainland France, *Comptes Rendus. Géoscience*, 353, no. S1, 413–440, doi: 10.5802/crgeos.95.
- 456 Bertrand, G., P. Elsass, G. Wirsing, and A. Luz, 2006, Quaternary faulting in the Upper Rhine Graben revealed
457 by high-resolution multi-channel reflection seismic, *Comptes Rendus Geosci.*, 338, no. 8, 574–580, doi:
458 10.1016/j.crte.2006.03.012.
- 459 Bettinelli, P., J. P. Avouac, M. Flouzat, L. Bollinger, G. Ramillien, S. Rajaure, and S. Sapkota, 2008, Seasonal
460 variations of seismicity and geodetic strain in the Himalaya induced by surface hydrology, *Earth Planet.*
461 *Sci. Lett.*, 266, nos. 3–4, 332–344, doi: 10.1016/j.epsl.2007.11.021.
- 462 Blanpied, M. L., D. A. Lockner, and J. D. Byerlee, 1995, Frictional slip of granite at hydrothermal conditions, *J.*
463 *Geophys. Res. Solid Earth*, 100, no. B7, 13045–13064, doi: 10.1029/95JB00862.
- 464 Bommer, J. J., and H. Crowley, 2017, The Purpose and Definition of the Minimum Magnitude Limit in PSHA
465 Calculations, *Seismol. Res. Lett.*, 88, no. 4, 1097–1106, doi: 10.1785/0220170015.
- 466 Bonjer, K.-P., 1997, Seismicity pattern and style of seismic faulting at the eastern borderfault of the southern
467 Rhine Graben, *Tectonophysics*, 275, nos. 1–3, 41–69, doi: 10.1016/S0040-1951(97)00015-2.
- 468 Calais, E., T. Camelbeeck, S. Stein, M. Liu, and T. J. Craig, 2016, A new paradigm for large earthquakes in
469 stable continental plate interiors, *Geophys. Res. Lett.*, 43, no. 20, 10,621–10,637, doi:
470 10.1002/2016GL070815.
- 471 Cara, M. et al., 2015, SI-Hex: a new catalogue of instrumental seismicity for metropolitan France, *Bull. la*
472 *Société Géologique Fr.*, 186, no. 1, 3–19, doi: 10.2113/gssgfbull.186.1.3.
- 473 Carter, N. L., and F. D. Hansen, 1983, Creep of rock salt, *Tectonophysics*, 92, no. 4, 275–333, doi:
474 10.1016/0040-1951(83)90200-7.
- 475 Chartier, T., O. Scotti, C. Clément, H. Jomard, and S. Baize, 2017, Transposing an active fault database into a
476 fault-based seismic hazard assessment for nuclear facilities – Part 2: Impact of fault parameter
477 uncertainties on a site-specific PSHA exercise in the Upper Rhine Graben, eastern France, *Nat. Hazards*
478 *Earth Syst. Sci.*, 17, no. 9, 1585–1593, doi: 10.5194/nhess-17-1585-2017.
- 479 Churchill, R. M., M. J. Werner, J. Biggs, and Å. Fagereng, 2022, Afterslip Moment Scaling and Variability From
480 a Global Compilation of Estimates, *J. Geophys. Res. Solid Earth*, 127, no. 4, doi: 10.1029/2021JB023897.

Code de champ modifié

Mis en forme : Anglais (États-Unis)

- 481 Craig, T. J., E. Calais, L. Fleitout, L. Bollinger, and O. Scotti, 2016, Evidence for the release of long-term
482 tectonic strain stored in continental interiors through intraplate earthquakes, *Geophys. Res. Lett.*, 43, no.
483 13, 6826–6836, doi: 10.1002/2016GL069359.
- 484 Craig, T. J., K. Chanard, and E. Calais, 2017, Hydrologically-driven crustal stresses and seismicity in the New
485 Madrid Seismic Zone, *Nat. Commun.*, 8, no. 1, 2143, doi: 10.1038/s41467-017-01696-w.
- 486 Danciu, L. et al., 2021, The 2020 update of the European Seismic Hazard Model: Model Overview.
487 <https://doi.org/10.3929/ethz-b-000590386>
- 488 Dieterich, J. H., 1979, Modeling of Rock Friction Experimental Results and Constitutive Equations, *J. Geophys.*
489 *Res.*, 84, no. B5, 2161–2168.
- 490 Doubre, C., M. Meghraoui, F. Masson, S. Lambotte, H. Jund, M. Bès de Berc, and M. Grunberg, 2022,
491 Seismotectonics in Northeastern France and neighboring regions, *Comptes Rendus. Géoscience*, 353, no.
492 S1, 153–185, doi: 10.5802/crgeos.80.
- 493 Drouet, S., G. Ameri, K. Le Dortz, R. Secanell, and G. Senfaute, 2020, A probabilistic seismic hazard map for
494 the metropolitan France, *Bull. Earthq. Eng.*, 18, no. 5, 1865–1898, doi: 10.1007/s10518-020-00790-7.
- 495 Fäh, D. et al., 2009, The 1356 Basel earthquake: an interdisciplinary revision, *Geophys. J. Int.*, 178, no. 1, 351–
496 374, doi: 10.1111/j.1365-246X.2009.04130.x.
- 497 Felzer, K. R., 2008, Calculating California seismicity rates.
- 498 Freymark, J., J. Sippel, M. Scheck-Wenderoth, K. Bär, M. Stiller, J.-G. Fritsche, and M. Kracht, 2017, The deep
499 thermal field of the Upper Rhine Graben, *Tectonophysics*, 694, 114–129, doi: 10.1016/j.tecto.2016.11.013.
- 500 Fuhrmann, T., M. Caro Cuenca, A. Knöpfler, F. J. van Leijen, M. Mayer, M. Westerhaus, R. F. Hanssen, and B.
501 Heck, 2015, Estimation of small surface displacements in the Upper Rhine Graben area from a combined
502 analysis of PS-InSAR, levelling and GNSS data, *Geophys. J. Int.*, 203, no. 1, 614–631, doi:
503 10.1093/gji/ggv328.
- 504 Grünthal, G., D. Stromeyer, C. Bosse, F. Cotton, and D. Bindi, 2018, The probabilistic seismic hazard
505 assessment of Germany—version 2016, considering the range of epistemic uncertainties and aleatory
506 variability, *Bull. Earthq. Eng.*, 16, no. 10, 4339–4395, doi: 10.1007/s10518-018-0315-y.
- 507 Guillou-Frottier, L., C. Carré, B. Bourguin, V. Bouchot, and A. Genter, 2013, Structure of hydrothermal
508 convection in the Upper Rhine Graben as inferred from corrected temperature data and basin-scale
509 numerical models, *J. Volcanol. Geotherm. Res.*, 256, 29–49, doi: 10.1016/j.jvolgeores.2013.02.008.
- 510 Heidbach, O. et al., 2018, The World Stress Map database release 2016: Crustal stress pattern across scales,
511 *Tectonophysics*, 744, 484–498, doi: 10.1016/j.tecto.2018.07.007.
- 512 Heidbach, O., M. Rajabi, K. Reiter, M. O. Ziegler, and WSM Team, 2016, World Stress Map Database Release
513 2016, V. 1.1. GFZ Data Services. <https://doi.org/10.5880/WSM.2016.001>
- 514 Henrion, E., F. Masson, C. Doubre, P. Ulrich, and M. Meghraoui, 2020, Present-day deformation in the Upper
515 Rhine Graben from GNSS data, *Geophys. J. Int.*, 223, no. 1, 599–611, doi: 10.1093/gji/ggaa320.
- 516 Hinsken, S., K. Ustaszewski, and A. Wetzel, 2007, Graben width controlling syn-rift sedimentation: the
517 Palaeogene southern Upper Rhine Graben as an example, *Int. J. Earth Sci.*, 96, no. 6, 979–1002, doi:
518 10.1007/s00531-006-0162-y.
- 519 Jomard, H., E. M. Cushing, L. Palumbo, S. Baize, C. David, and T. Chartier, 2017, Transposing an active fault
520 database into a seismic hazard fault model for nuclear facilities – Part 1: Building a database of potentially
521 active faults (BDFa) for metropolitan France, *Nat. Hazards Earth Syst. Sci.*, 17, no. 9, 1573–1584, doi:
522 10.5194/nhess-17-1573-2017.
- 523 Kraft, T., and N. Deichmann, 2014, High-precision relocation and focal mechanism of the injection-induced
524 seismicity at the Basel EGS, *Geothermics*, 52, 59–73, doi: 10.1016/j.geothermics.2014.05.014.

- 525 Leonard, M., 2010, Earthquake Fault Scaling: Self-Consistent Relating of Rupture Length, Width, Average
526 Displacement, and Moment Release, *Bull. Seismol. Soc. Am.*, 100, no. 5A, 1971–1988, doi:
527 10.1785/0120090189.
- 528 Lutz, M., and M. Cleintuar, 1999, Geological results of a hydrocarbon exploration campaign in the southern
529 Upper Rhine Graben (Alsace Centrale, France), *Bull. für Angew. Geol.*, 4, 3–80, doi:
530 <http://doi.org/10.5169/seals-221515>.
- 531 Manchuel, K., P. Traversa, D. Baumont, M. Cara, E. Nayman, and C. Durouchoux, 2018, The French seismic
532 CATalogue (FCAT-17), *Bull. Earthq. Eng.*, 16, no. 6, 2227–2251, doi: 10.1007/s10518-017-0236-1.
- 533 Marsan, D., M. Bouchon, B. Gardonio, H. Perfettini, A. Socquet, and B. Enescu, 2017, Change in seismicity
534 along the Japan trench, 1990-2011, and its relationship with seismic coupling, *J. Geophys. Res. Solid
535 Earth*, 122, no. 6, 4645–4659, doi: 10.1002/2016JB013715.
- 536 Mayer-Rosa, D., and B. Cadiot, 1979, A review of the 1356 Basel earthquake: Basic data, *Tectonophysics*, 53,
537 nos. 3–4, 325–333, doi: 10.1016/0040-1951(79)90077-5.
- 538 Mazzotti, S. et al., 2021, FMHex20: An earthquake focal mechanism database for seismotectonic analyses in
539 metropolitan France and bordering regions, *BSGF - Earth Sci. Bull.*, 192, 10, doi: 10.1051/bsgf/2020049.
- 540 Michel, S., J. Avouac, R. Jolivet, and L. Wang, 2018, Seismic and Aseismic Moment Budget and Implication for
541 the Seismic Potential of the Parkfield Segment of the San Andreas Fault, *Bull. Seismol. Soc. Am.*, 108, no.
542 1, 19–38, doi: 10.1785/0120160290.
- 543 Michel, S., R. Jolivet, C. Rollins, J. Jara, and L. Dal Zilio, 2021, Seismogenic Potential of the Main Himalayan
544 Thrust Constrained by Coupling Segmentation and Earthquake Scaling, *Geophys. Res. Lett.*, 48, no. 13, 1–
545 10, doi: 10.1029/2021GL093106.
- 546 Molnar, P., 1979, Earthquake Recurrence Intervals and Plate Tectonics, 115–133.
547 <https://doi.org/10.1785/BSSA0690010115>
- 548 Nivière, B., A. Bruestle, G. Bertrand, S. Carretier, J. Behrmann, and J.-C. Gourry, 2008, Active tectonics of the
549 southeastern Upper Rhine Graben, Freiburg area (Germany), *Quat. Sci. Rev.*, 27, nos. 5–6, 541–555, doi:
550 10.1016/j.quascirev.2007.11.018.
- 551 Oleskevich, D. A., R. D. Hyndman, and K. Wang, 1999, The updip and downdip limits to great subduction
552 earthquakes: Thermal and structural models of Cascadia, south Alaska, SW Japan, and Chile, *J. Geophys.
553 Res. Solid Earth*, 104, no. B7, 14965–14991, doi: 10.1029/1999JB900060.
- 554 Pena-Castellnou, S. et al., 2023, First evidence of surface rupturing earthquakes in the eastern Rhine Graben
555 Boundary Fault (Germany). <https://dx.doi.org/10.2139/ssrn.4472340>
- 556 Rollins, C., and J. Avouac, 2019, A Geodesy- and Seismicity-Based Local Earthquake Likelihood Model for
557 Central Los Angeles, *Geophys. Res. Lett.*, 46, no. 6, 3153–3162, doi: 10.1029/2018GL080868.
- 558 Rotstein, Y., and M. Schaming, 2011, The Upper Rhine Graben (URG) revisited: Miocene transtension and
559 transpression account for the observed first-order structures, *Tectonics*, 30, no. 3, doi:
560 10.1029/2010TC002767.
- 561 Rouland, D., H. Haessler, K. P. Bonjer, B. Gilg, D. Mayer-Rosa, and N. Pavoni, 1983, The Sierentz Southern-
562 Rhinegraben Earthquake of July 15, 1980. Preliminary Results, in *Developments in Solid Earth
563 Geophysics*, 441–446, doi: 10.1016/B978-0-444-99662-6.50086-1
- 564 Ruina, A., 1983, Slip instability and state variable friction laws, *J. Geophys. Res. Solid Earth*, 88, no. B12,
565 10359–10370, doi: 10.1029/JB088iB12p10359.
- 566 Steer, P., M. Simoes, R. Cattin, and J. B. H. Shyu, 2014, Erosion influences the seismicity of active thrust faults,
567 *Nat. Commun.*, 5, no. 1, 5564, doi: 10.1038/ncomms6564.
- 568 Stirling, M., T. Goded, K. Berryman, and N. Litchfield, 2013, Selection of Earthquake Scaling Relationships for
569 Seismic-Hazard Analysis, *Bull. Seismol. Soc. Am.*, 103, no. 6, 2993–3011, doi: 10.1785/0120130052.

Mis en forme : Anglais (États-Unis)

570 Stucchi, M. et al., 2013, The SHARE European Earthquake Catalogue (SHEEC) 1000–1899, *J. Seismol.*, 17, no.
571 2, 523–544, doi: 10.1007/s10950-012-9335-2.

572 Traversa, P., D. Baumont, K. Manchuel, E. Nayman, and C. Durouchoux, 2018, Exploration tree approach to
573 estimate historical earthquakes Mw and depth, test cases from the French past seismicity, *Bull. Earthq.*
574 *Eng.*, 16, no. 6, 2169–2193, doi: 10.1007/s10518-017-0178-7.

575 Wells, D. L., and K. J. Coppersmith, 1994, New empirical relationships among magnitude, rupture length,
576 rupture width, rupture area, and surface displacement, *Bull. Seismol. Soc. Am.*, 84, no. 4, 974–1002, doi:
577 <https://doi.org/10.1785/BSSA0840040974>.

578 Weng, H., and H. Yang, 2017, Seismogenic width controls aspect ratios of earthquake ruptures, *Geophys. Res.*
579 *Lett.*, 44, no. 6, 2725–2732, doi: 10.1002/2016GL072168.

580 Wesnousky, S. G., 2006, Predicting the endpoints of earthquake ruptures, *Nature*, 444, no. 7117, 358–360, doi:
581 10.1038/nature05275.

582 Woessner, J. et al., 2015, The 2013 European Seismic Hazard Model: key components and results, *Bull. Earthq.*
583 *Eng.*, 13, no. 12, 3553–3596, doi: 10.1007/s10518-015-9795-1.

584 Zaliapin, I., and Y. Ben-Zion, 2013, Earthquake clusters in southern California I: Identification and stability, *J.*
585 *Geophys. Res. Solid Earth*, 118, no. 6, 2847–2864, doi: 10.1002/jgrb.50179.

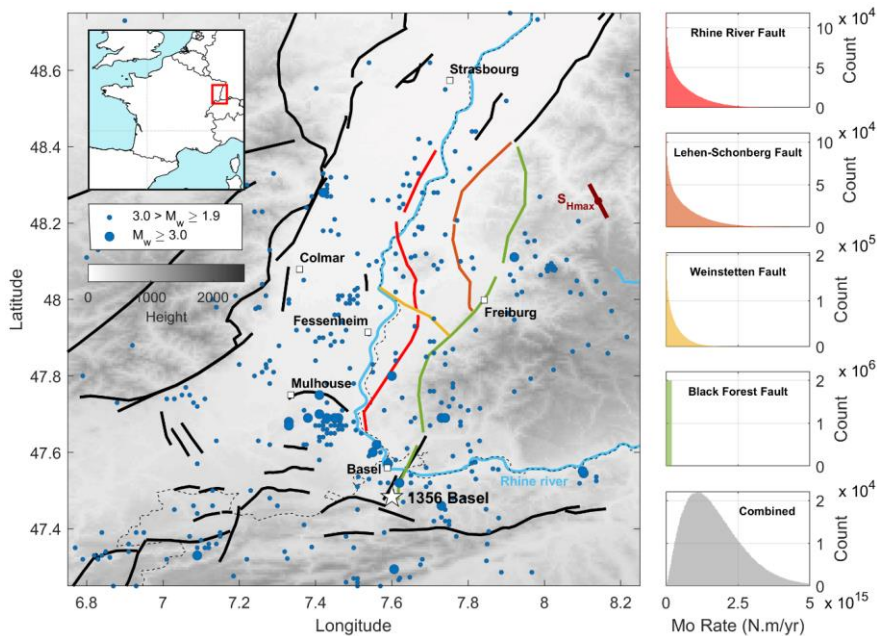
586

587

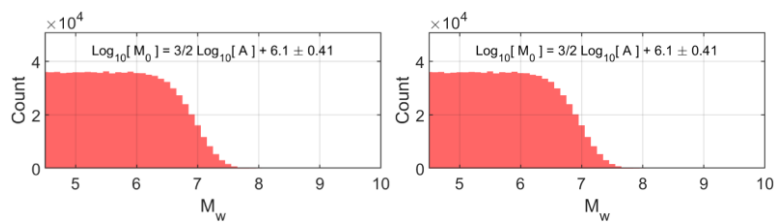
588

589

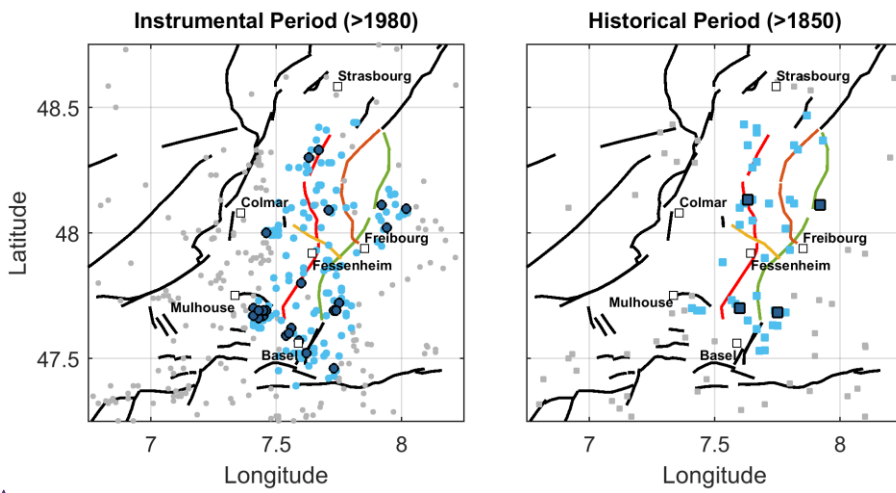
590



591
 592 **Figure 1:** (Left panel) Regional setting and seismicity of the Upper Rhine Graben (Drouet et al., 2020). Black lines are
 593 faults while colored ones are the faults taken into account in this study. The fault network geometry is based on the
 594 B DFA database (Jomard et al., 2017) and Nivière et al. (2008). Blue dots are epicenters of $M_w > 2.2$ earthquakes since
 595 1994. The white star indicates the 1356 Basel earthquake (magnitude ranging from $M6.5 \pm 0.5$ (Manchuel et al., 2017)
 596 to $M6.9 \pm 0.2$ (Fäh et al., 2009)). The brown bar indicates the approximate orientation of the maximum horizontal
 597 compressional stress (S_{Hmax}) (Heidbach et al., 2016, 2018). The thin dashed black line is the border between France
 598 and Germany. The nuclear powerplant of Fessenheim and the main cities are indicated by white squares. (Right panels)
 599 Moment deficit rate PDFs (expressed in counts) are given for each of the four considered faults (colors are indicative of the faults in the left panel),
 600 and of their combination (in grey).



601
 602 **Figure 2:** PDF of M_w considering the along-dip moment-area scaling law of earthquakes from Leonard (2010). Note
 603 that the area from the Black Forest Fault is not included, as its loading rate is assumed equal to 0 mm/yr.



604

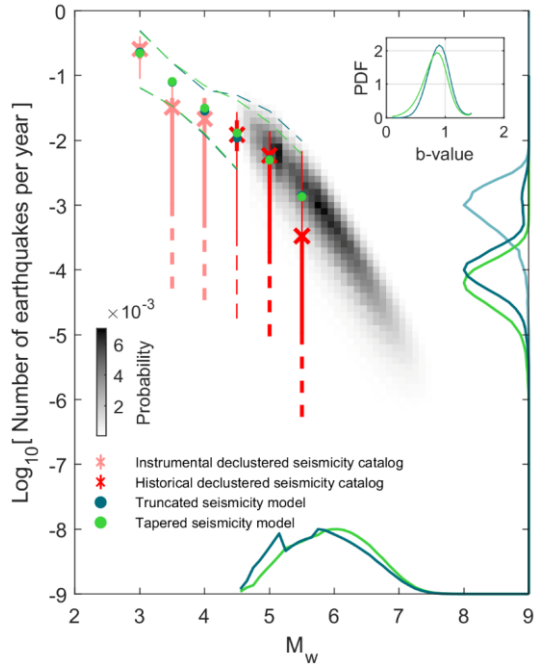
605 **Figure 3:** Earthquake selection for the instrumental (>1994) and historical (>1850) periods. Gray dots and squares
 606 indicate all earthquakes with $M_c = 2.2$ and 3.2 for the instrumental and historical catalogs, respectively. Light blue
 607 dots and squares indicate earthquakes taken into account for the seismogenic potential analysis. Dark blue dots and
 608 squares indicate $M_w \geq 2.8$ and 2.75 and $4.25-3$ earthquakes taken into account for the seismogenic potential analysis.

609

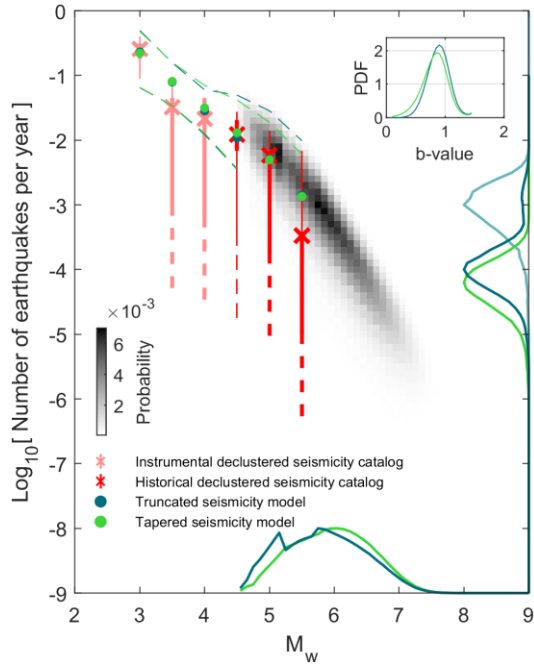
610

Mis en forme : Police :

611



612



613 Figure 4: Seismogenic potential of the URG using all constraints: moment budget, observed magnitude-frequency
614 distribution, and moment area scaling law. The rate of occurrence of historical and instrumental earthquakes, within
615 their observation periodsperiod, are indicated by red and pink crosses and error bars, respectively. Thick and thin
616 error bars indicate the 15.9-84.1% (1-sigma) and 2.3-97.7% (2-sigma) quantilesquantile of the MFDs. Dashed lines show
617 the spread of possible MFDs for the 2500 catalogs randomly generated to explore uncertainties. The green and blue
618 colors are associated withto the tapered and truncated long-term seismicity modelsmodel. Green and blue dots show
619 the meansmean of the marginal PDF forof the long-term seismicity. DashedGreen and blue dashedlines indicate the
620 spread of the best 1% best seismicity models. The marginal probabilities of M_{max} , $P_{M_{max}}$, are indicated by the solid
621 lines on the M_w axis. They have been normalized so that their amplitude is equal to one instead of 0.60 and 0.59 for the
622 tapered and truncated models, respectively. Green and dark blue lines on the earthquake frequency axis indicate the
623 probability of the rate of events, τ , with magnitude $M_w = M_{Mode}$, thus $P(\tau | M_w = M_{Mode})$, with $M_{Mode}=6.05$ 1 and
624 5.758 for the tapered and truncated models, respectively, considering all magnitudes in the seismicity models and not
625 only the recurrence rate of M_{max} . They have also been normalized and their peaks were initially at 1.13 and 1.17 for
626 the tapered and truncated models, respectively. The Hight blue line on the earthquake frequency axis indicates
627 $P(\tau_{max} | M_{max} = 5.875)$ (only for the truncated seismicity model only) and is normalized so that its amplitude equals
628 one instead of 1.19. The top-right inset shows the marginal probability of the b-value. Note that the seismicity MFDs
629 shown in the figure are not in the cumulative form.

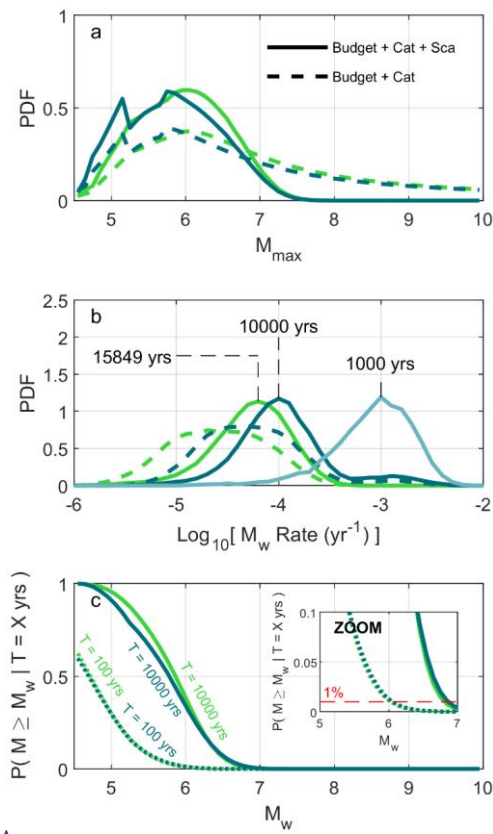
Mis en forme : Police :

Mis en forme : Police :

Mis en forme : Police :

Mis en forme : Police :

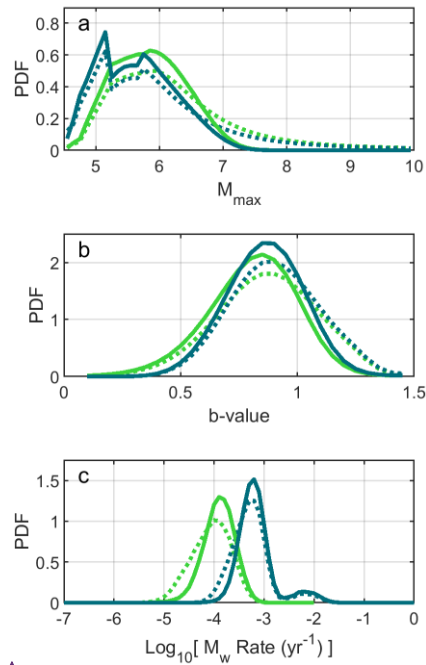
Mis en forme : Police :



Mis en forme : Police :

630

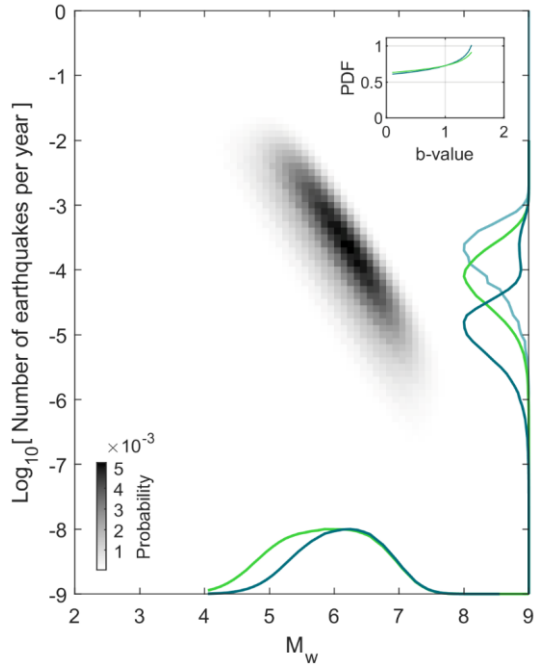
631 **Figure 5:** (a) Evolution of the marginal PDF of M_{max} when adding the moment-area scaling law constraint. The green
632 and blue colors in the figure are associated with the tapered and truncated long-term seismicity models. (b)
633 Same as (a) but for the marginal PDF of the recurrence time of events: $P(\tau | M_w = 6.1)$ and $P(\tau | M_w = 5.8)$
634 for the tapered and truncated models (dark blue and green lines), respectively, and $P(\tau_{max} | M_{max} = 5.875)$
635 shown only for the truncated model (solid light blue line). (c) Probability of occurrence
636 of earthquakes with a magnitude larger than M_w over a period of X yrs. We show the probability of occurrence of
637 such events for the 100 yrs and 10,000 yrs time periods. In (a), (b) and (c), dotted lines represent the marginal PDFs
638 considering both the moment budget and seismicity catalog constraint, the dashed lines indicate the PDFs when adding
639 the earthquake scaling constraint is added. The inset in (c) is a zoom of the panel. The 1% probability of exceedance
640 over a time period of 100 yrs is a typical order of magnitude for nuclear applications in France.



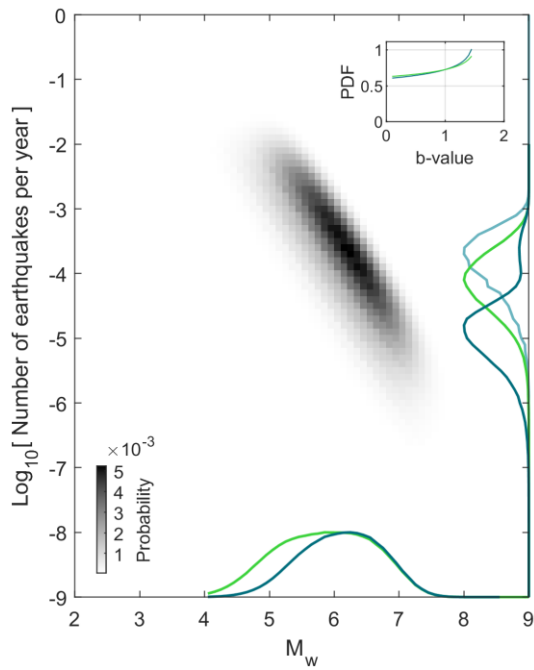
641

642 **Figure 6:** Results using the declustering method from Zaliapin and Ben-Zion (2013) instead of Marsan et al. (2017)
 643 (Text S2). In this scenario, no probabilities of events to be mainshocks are defined. (a) M_{max} PDF. (b) b-value PDF. (c)
 644 $P(\tau | M_w = M_{Mode})$ PDF. Solid lines correspond to the results using all constraints while the dotted lines use-only use
 645 the moment budget and earthquake catalogs constraints. Green and blue lines correspond to the tapered and truncated
 646 models, respectively. The results shown here are the ones taking a b-value equal to 1 for Zaliapin and Ben-Zion (2013)
 647 declustering method. The results for b-values of 0.5 and 1.5 are also shown in Figure S154 and are relatively similar to
 648 the ones obtained using a b-values of 1.0.

649



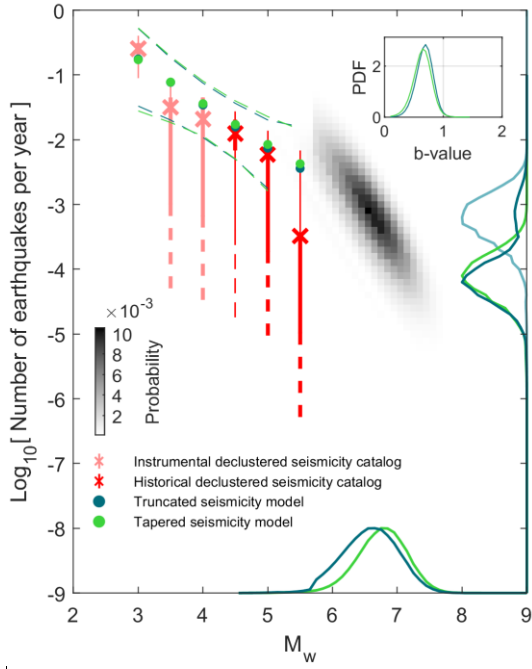
650



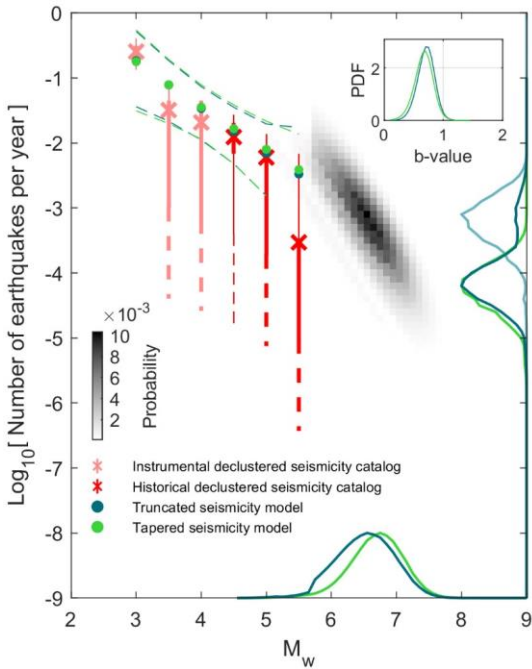
651 Figure 7: Same as Figure 4 but only considering ~~only~~ the constraints for~~on~~ the moment budget, the moment-area scaling
652 law, and the one on M_{max} frequency considering the time period of the catalog (which serves as a lower bound constraint
653 for~~to~~ M_{max} ; Section 5.2; Approach 2 from Michel et al., 2018). The marginal probabilities $P_{M_{max}}$ have been normalized
654 so that their amplitude is equal to one instead of 0.46 and 0.58 for the tapered and truncated models, respectively. The
655 same is true- for $P(\tau | M_w = M_{Mode})$, which were initially of 0.85 and 0.81 of amplitude, and $P(\tau_{max} | M_{max} = 6.3)$
656 (only for the truncated seismicity model only) which peaked at an amplitude of 0.85 of amplitude.

Mis en forme : Police :

657



658



659 Figure 8: Same as Figure 2 but considering a strike-slip slip rate component equivalent to ~~46.64~~48 times the dip-slip
660 estimate, and assuming the Black Forest Fault maximum long-term vertical slip rate is 0.18 mm/yr (as proposed by
661 Jomard et al., 2017). Leonard et al.'s (2010) strike-slip moment-area scaling law is used here for the scaling law
662 constraint, even though it is very similar to the dip-slip version. The marginal probabilities $P_{M_{max}}$ have been normalized
663 so that their amplitude is equal to one instead of 1.02 and 0.88 for the tapered and truncated models, respectively. The
664 same is true for $P(\tau | M_w = M_{Mode})$ which were initially of 1.15 and 1.13 of amplitude, and $P(\tau_{max} | M_{max} = 6.6)$ (only
665 for the truncated seismicity model only) which peaked at an amplitude of 1.17 of amplitude.

666

667 **Table 1: Fault parameters.** \mathcal{U} and \mathcal{N} stands for uniform and normal distribution. The PDFs of each of ~~these~~
668 parameters and the resulting moment deficit rate ~~for~~ each fault are shown in Figure S32 to S65.

Fault Name	Segment Name (from BDFA)	Dip (°)	Length (km)	Slip-Rate (mm/yr)	Seismogenic zone down-dip extent (km)	Evaporite layer thickness (km)
Rhine River Fault	FRR-1	$\mathcal{U}(50,80)$	$\mathcal{N}(35,2)$	$\mathcal{U}(0,0.07)$	(1) Uniform from 0 to 6 km <u>in</u> depth. (2) Linearly decreasing	$\mathcal{U}(0,2)$
	FRR-2	$\mathcal{U}(50,80)$	$\mathcal{N}(25,2)$			
	FRR-3	$\mathcal{U}(55,85)$	$\mathcal{N}(20,2)$			
Black Forest Fault	FFN-1	$\mathcal{U}(35,75)$	$\mathcal{N}(20,5)$	0	from 6 to 18 km depth.	
	FFN-2	$\mathcal{U}(40,80)$	$\mathcal{N}(50,2)$			
	FFN-3	$\mathcal{U}(35,75)$	$\mathcal{N}(35,2)$			
Lehen-Schonberg		$\mathcal{U}(40,80)$	$\mathcal{N}(54,2)$	$\mathcal{U}(0,0.1)$	Does not apply to the Black Forest Fault as its loading rate is assumed equal to 0 mm/yr	
Weinstetten		$\mathcal{U}(40,80)$	$\mathcal{N}(15,2)$	$\mathcal{U}(0,0.17)$		

669
670
671

672

Table 2: Summary of the results considering the different scenarios tested from section 4 to 5.3.

<u>Scenarios</u>	<u>Modes of M_{max}</u>	<u>99% probability that M_{max} is below magnitude M_w</u>	<u>Mode of $P(\tau M_w = M_{Mode})$</u>
<u>Rhine River Fault + Lehen-Schonberg Fault + Weinstetten Fault</u> <u>Dip-Slip Only</u> <u>Marsan et al. (2017) Declus.</u> (Section 4 / Fig. 4 and 5)	<u>Tapered Model</u> <u>M_w 6.1</u> <u>Truncated Model</u> <u>M_w 5.2 and 5.8</u>	<u>Tapered Model</u> <u>M_w 7.3</u> <u>Truncated Model</u> <u>M_w 7.3</u>	<u>Tapered Model</u> <u>$\tau = 16,000$ yrs</u> <u>Truncated Model</u> <u>$\tau = 2,000$ and $10,000$ yrs</u>
<u>Rhine River Fault + Lehen-Schonberg Fault + Weinstetten Fault</u> <u>Dip-Slip Only</u> <u>Zaliapin and Ben-Zion (2013) Declus.</u> (Section 5.1 / Fig. 6)	<u>Tapered Model</u> <u>M_w 5.9</u> <u>Truncated Model</u> <u>M_w 5.2 and 5.8</u>	<u>Tapered Model</u> <u>M_w 7.2</u> <u>Truncated Model</u> <u>M_w 7.1</u>	<u>Tapered Model</u> <u>$\tau = 8,000$ yrs</u> <u>Truncated Model</u> <u>$\tau = 1,600$ and $8,000$ yrs</u>
<u>Rhine River Fault + Lehen-Schonberg Fault + Weinstetten Fault</u> <u>Dip-Slip Only</u> <u>Marsan et al. (2017) Declus.</u> <u>Loose catalog constraint</u> <u>(Approach 2 from Michel et al., 2018)</u> (Section 5.2 / Fig. 7)	<u>Tapered Model</u> <u>M_w 5.9</u> <u>Truncated Model</u> <u>M_w 6.3</u>	<u>Tapered Model</u> <u>M_w 7.4</u> <u>Truncated Model</u> <u>M_w 7.4</u>	<u>Tapered Model</u> <u>$\tau = 12,500$ yrs</u> <u>Truncated Model</u> <u>$\tau = 63,000$ yrs</u>
<u>Rhine River Fault + Lehen-Schonberg Fault + Weinstetten Fault + Black Forest Fault</u> <u>Strike- and Dip-Slip</u> <u>Marsan et al. (2017) Declus.</u> (Section 5.3 / Fig. 8)	<u>Tapered Model</u> <u>M_w 6.8</u> <u>Truncated Model</u> <u>M_w 6.6</u>	<u>Tapered Model</u> <u>M_w 7.6</u> <u>Truncated Model</u> <u>M_w 7.5</u>	<u>Tapered Model</u> <u>$\tau = 16,000$ yrs</u> <u>Truncated Model</u> <u>$\tau = 16,000$ yrs</u>

673

674